HHS Public Access

Author manuscript

Biomater Sci. Author manuscript; available in PMC 2022 January 26.

Published in final edited form as:

Biomater Sci. 2021 January 26; 9(2): 496–505. doi:10.1039/d0bm00897d.

Tb-doped Core-shell-shell nanophosphors for enhanced X-ray induced luminescence and sensitization of radiodynamic therapy

Yufu Ren[a], **Justin G. Rosch**[a], **Madeleine R. Landry**[a], **Hayden Winter**[b], **Syamantak Khan**[c], **Guillem Pratx**[c], **Conroy Sun**[a,d]

[a]Department of Pharmaceutical Sciences, College of Pharmacy, Oregon State University, 2730 SW Moody Ave, Portland, OR 97201, USA.

[b]Department of Chemistry, College of Liberal Arts & Sciences, Portland State University, 1719 SW 10th Ave, Portland, OR 97201, USA.

[c]Department of Radiation Oncology, School of Medicine, Stanford University, 300 Pasteur Drive, Stanford, CA 94305, USA.

[d]Department of Radiation Medicine, School of Medicine, Oregon Health & Science University, 3181 S.W. Sam Jackson Park Road, Portland, OR 97239, USA.

Abstract

The development of radiation responsive materials, such as nanoscintillators, enables a variety of exciting new theranostic applications. In particular, the ability of nanophosphors to serve as molecular imaging agents in novel modalities, such as X-ray luminescence computed tomography (XLCT), has gained significant interest recently. Here, we present a radioluminescent nanoplatform consisting of Tb-doped nanophosphors with an unique core/shell/shell (CSS) architecture for improved optical emission under X-ray excitation. Owing to the spatial confinement and separation of luminescent activators, these CSS nanophosphors exhibited bright optical luminescence upon irradiation. In addition to standard physiochemical characterization, these CSS nanophosphors were evaluated for their ability to serve as energy mediators in X-ray stimulated photodynamic therapy, also known as radiodynamic therapy (RDT), through attachment of a photosensitizer, rose bengal (RB). Furthermore, cRGD peptide was used as a model targeting agent against U87 MG glioblastoma cells. In vitro RDT efficacy studies suggested the RGD-CSS-RB in combination with X-ray irradiation could induce enhanced DNA damage and increased cell killing, while the nanoparticles alone are well tolerated. These studies support the utility of CSS nanophosphors and warrants their further development for theranostic applications.

Graphical Abstract

sunc@ohsu.edu.

Electronic Supplementary Information (ESI) available. See DOI: 10.1039/d0bm00897d

Conflicts of interest

The authors declare no competing financial interest.

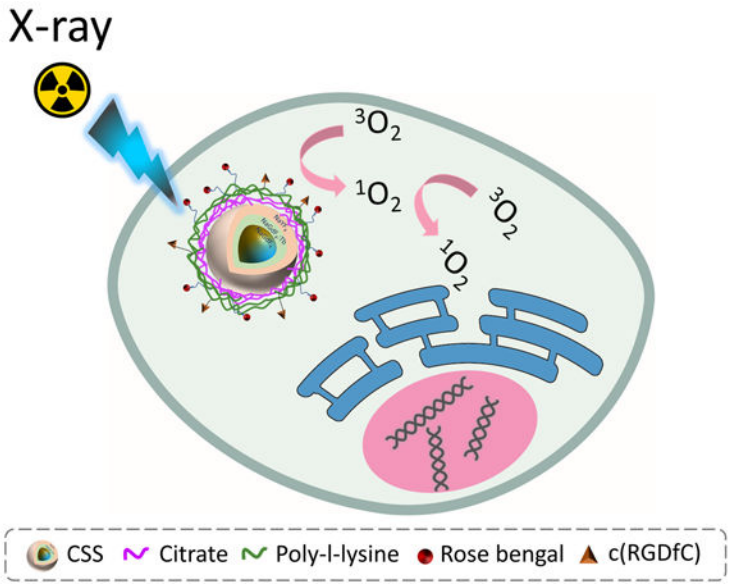

Tb doped core/shell/shell nanophosphor exhibits robust X-ray luminescence and potential in radiodynamic therapy.

Introduction

Lanthanide-doped nanophosphors capable of efficiently down-converting X-rays to visible light photons have been investigated for radioluminescent (RL) imaging and therapeutic applications.[1–4] Of particular interest are near infrared (NIR) emitting nanoparticles that exploit the optical window of biological tissue.[5] Development of these X-ray-in NIR-out nanoparticles has sparked interest in multimodal imaging techniques such as X-ray luminescence computed tomography (XLCT).[6, 7] In therapeutic applications, RL nanophosphors have drawn significant attention as energy mediators enabling X-ray induced photodynamic therapy (PDT), also known as radiodynamic therapy (RDT).[8–10]

In conventional PDT, photosensitizers under light irradiation produce reactive oxygen species (ROS) to induce irreversible cancer cell damage via apoptosis-mediated cell injury.[11, 12] In comparison to drug based therapies, PDT possesses many advantages, such as minimal side effects, spatiotemporal selectivity, low drug resistance, and good therapeutic efficacy.[11, 13] However, the limited tissue penetration depth of the external light has greatly hindered the widespread clinical application of the PDT. By combining X-ray induced radiation therapy and PDT to eliminate incident photon scattering there is a potential to improve the therapeutic outcome of malignant tumors located in deep tissue.[14] Conceptually, this usually involves an energy transduction process, as the nanoscintillators internalized by tumor tissue can convert the high energy X-rays into visible light and subsequently activate a photosensitizer (PS) for the generation of cytotoxic ROS.

Of particular interest in this application has been Tb-doped $NaGdF_4$ based nanophosphors due to the overlap between the green emission of Tb^{3+} and the absorption of certain PSs, such as rose bengel (RB) and merocyanine 540 (MC540). Moreover, the high-Z element, Gd

not only possesses high X-ray mass absorption coefficient, but also serves as the intermediate to contribute to the down-conversion excitation of light-emitting lanthanide ions in a Gd^{3+}-containing host matrix.[15–18] Benefiting from intrinsic low phonon energy of the $NaGdF_4$ host nanocrystals, the undesired non-radiative bridging can be greatly mitigated.[19–21] Interestingly, a recent study has demonstrated that the $NaGdF_4$ nanocrystals can also perform as a contrast agent for magnetic resonance (MR) angiography, largely attributed to their significant r_1 longitudinal relaxivity and good chemical stability in a physiological environment.[22]

To design and construct a nanoprobe for RL imaging or RDT applications, the first step is to prepare the nanoparticles with strong scintillation properties. As noted, we and others have investigated X-ray excitable bioimaging probes for enhanced spatial resolution and deep tissue detection capability.[3, 23–26] XLCT has been demonstrated using different inorganic scintillators, such as rare earth oxides $Gd_2O_3:Eu^{3+}$ and oxysulfides $Gd_2O_2S:Eu^{3+}$.[6, 7, 27] However, due to the lack of solution based synthetic approaches, these types of scintillators frequently have a relatively large size distribution, which may result in varied biodistribution. For most in vivo applications, nanoscintillators with size distribution below 200 nm and biologically inert surface functionality, to increase circulation time and tumoral uptake, are favorable.[9] For instance, Ma et al. reported persistent luminescencing ZnS:Cu in combination with tetrabromorhodamine-123 (TBrRh123) to greatly enhance the cancer cell killing under X-ray irradiation (2 Gy).[28] In other reports, nanoparticles consisting of an SrAl2O4:Eu (SAO) core and MC540 loaded mesoporous silica shell were demonstrated to deliver significant damage to radioresistant cancer cells and induce complete tumor regression upon a low dose of X-ray administration (0.5 Gy).[29] Alternatively, rose bengel (RB) conjugated Zn- and Mn-incorporated silica (ZSM) and GC exhibited excellent radiosensitization leading to a strong inhibitory effect on tumor growth under low-dose X-ray irradiation.[30, 31]

A priority for both RL imaging probe development and RDT efficacy is the synthesis of nanoparticles with large X-ray absorption cross-section and high RL efficiency.[32] In general, low luminescence efficiency associated with lanthanide-doped nanophosphors is related to excited state quenching caused by the dipole-dipole coupling of lanthanide activators to the vibrational mode of the environment leading to undesired excitation energy migration to the surfaces and irreversible energy loss.[33, 34] Therefore, the most common strategy to boost the luminescence output of lanthanide-doped nanophosphors is to grow a luminescent inert shell over the active core. More recently, a new strategy was proposed to further improve the luminescence efficiency of lanthanide-doped upconversion nanoparticles by confining the luminescent emitters in an epitaxially grown shell.[35, 36] Based on this concept, the nanoparticle structured with core/shell/shell geometry was designed and the luminescent emitter ions were spatially distributed in the inner shell. As a result, the spatially confined emitter ions can generate an energy concentration zone and promote the energy transfer efficiency, which leads to enhanced luminescence emission.[35] Furthermore, concentrating the luminescent emitters in the region near the nanoparticle surface can promote the Förster resonance energy transfer (FRET) efficiency and result in improved singlet oxygen ($^1O_2$) generation.[37, 38] Taken together, the core/shell/shell nanophosphor not only exhibits

enhanced luminescence efficiency but can also improve the FRET coupling, making it a highly promising platform for potential RDT applications.

Here, we synthesized sub-20 nm $NaREY_4$ based core/shell/shell (CSS) nanophosphors with luminescent activators (Tb^{3+}) spatially confined in the interior shell. Following the assessment of their scintillation properties, the CSS nanophosphors were further modified with RB and cyclic RGD peptide. The as-prepared RGD-CSS-RB nanoconjugate displayed high cellular uptake *in vitro* and intracellular ROS generation. Moreover, upon combination with X-ray irradiation, the RGD-CSS-RB can induce significant cell death and DNA damage.

Results and discussion

The detailed synthesis procedure of $NaGdF_4$@$NaGdF_4$: Tb@$NaYF_4$ core/shell/shell nanoparticles, surface modification, and the bioconjugation chemistry are discussed in the experimental section. In short, the $NaGdF_4$@$NaGdF_4$: Tb@$NaYF_4$ CSS nanoparticles were synthesized by a modified co-precipitation strategy which involves the sequential epitaxial shell growth on the $NaGdF_4$ seeds.[39] Next, the electrostatic layer-by-layer deposition technique was employed to coat the nanoparticles with the poly-l-lysine (PLL), carrying primary amino groups. The RB and targeting peptide c(RGD) were then immobilized on the surface of the PLL coated nanoparticles via amide and thioether bond respectively. Upon exposure to the X-ray irradiation, the CSS nanoparticles can transfer the high-energy X-ray photons to visible light and subsequently stimulate RB to generate cytotoxic singlet oxygen ($^1O_2$), as illustrated in Schematic 1.

Transmission electron microscopy (TEM) images of the $NaGdF_4$ core nanoparticles showed a spherical morphology and uniform size distribution (Fig. 1a), with an average size of 8.4 nm. These $NaGdF_4$ seeds were shelled with two other layers to construct a core/shell/shell geometry. The interior shell was composed of Tb-doped $NaGdF_4$ nanocrystal ($NaGd_{1-x}F_4$: Tb_x) where x represents the varied concentration of Tb activators (x=0.10, 0.15, 0.20, 0.30 and 0.50), thus the interior shell could also be referred as the luminescent shell. After the epitaxial growth of the $NaGdF_4$: Tb layer, the $NaGdF_4$@$NaGdF_4$: Tb core/shell nanoparticles remained spherical in shape with high monodispersity and were approximately 12.6 nm in diameter (Figure 1b, e) as measured by dynamic light scattering (DLS).

To mediate surface quenching caused by resonant energy transfer among activator ions to the surface defects and ligands, a $NaYF_4$ inert shell was further deposited onto the $NaGdF_4$@$NaGdF_4$: Tb core/shell nanoparticle surface.[40] The resulting $NaGdF_4$@$NaGdF_4$:Tb@$NaYF_4$ core/shell/shell nanoparticles exhibited (Figure 1c, e) a mean size of approximately 15.8 nm and a sphere-like morphology, as a result of the successive isotropic shell growth. According to the DLS measurements (Figure 1e), the thickness of the $NaGdF_4$: Tb shell and $NaYF_4$ shell were about 2.1 nm and 1.5 nm respectively. The lattice fringe spacing from the high-resolution TEM (HRTEM) image of CSS nanoparticle (Figure 1d) was calculated to be 0.52 nm, which can be assigned to the (100) planes of the hexagonal phase $NaGdF_4$.[16] X-ray diffraction (XRD) pattern (Figure 1f) of the as-synthesized CSS nanoparticles displayed all the characteristic diffraction peaks of

β-$NaYF_4$ (PDF# 16–0334), which confirmed pure hexagonal structures of the core, interior shell and exterior shell.

To conjugate the photosensitizer and cell targeting peptide, the as-prepared CSS nanoparticles were treated with acid to remove the hydrophobic oleate ligands and the resulting ligand-free (LF) nanoparticles were subsequently coated with sodium citrate. As seen in Figure 1g, the zeta potential of the CSS nanoparticles shifted to −22.9 ± 7.9mV from 35.7 ± 8.3 mV after the citrate layering process. However, the highly negatively charged surface of the citrate capped CSS nanoparticles can result in limited cell uptake due to the electrostatic repulsive force generated by the negative charge on the cell membrane.[41] Thus, to alter the surface charge and introduce the amino conjugation sites, the citrate capped CSS (CSS@cit) nanoparticles were further complexed with poly-l-lysine (PLL), which has been widely studied as a coating agent for various cell labeling nanoplatforms.[42, 43] Briefly, the negatively charged CSS@cit nanoparticles electrostatically interacted with the positively charged PLL macromolecule to undergo a charge driven complexation process and form the CSS@Cit@PLL nanoparticle.[44] The positive surface charge (30.5 ± 5 mV) of the as-prepared CSS@Cit@PLL nanoparticle suggests the amino acids were successfully layered on the surface of the CSS nanoparticles.[45] In terms of overall size evolution, DLS results (Figure S1) revealed the average hydrodynamic diameter of CSS@Cit@PLL nanocomplexes increased to 72 nm, compared to the 53.9 nm for CSS@Cit and 32.4 nm for LF-CSS nanoparticles. Next, the photosensitizer RB was coupled with the CSS@Cit@PLL nanocomplexes by EDC/NHS chemistry to obtain the CSS-RB nanoconjugates. The positive surface charge of CSS-RB nanoconjugates decreased by approximately 8 mV (Figure 1g), which suggests the negatively charged RB molecules were covalently bonded with CSS nanoparticles. Also, the as-prepared CSS-RB nanoconjugates exhibited symmetrical size distribution centered around 120 nm without significant aggregation, according to the DLS measurement (Figure 1h). Last, the CSS-RB nanoconjugates were functionalized with thiol containing RGD peptides via sulfo-SMCC cross linking. The pink/red colored lyophilized RGD-CSS-RB nanoconjugates (Figure S2a) further support the efficient loading of the RB dye. The presence of RB and RGD on the surface of the RGD-CSS-RB nanoconjugates were then confirmed by the Fourier transform infrared (FT-IR) spectroscopy (Figure S2b).

The X-ray scintillation properties of the CSS nanoparticles were examined using a custom designed spectrometer (Stellarnet Inc) system coupled with X-ray irradiation (130 kV and 5 mA). As seen in Figure S3, the $NaGdF_4$@$NaGdF_4$:Tb@$NaYF_4$ core/shell/shell nanoparticles exhibited the typical Tb^{3+} emissions peaked at 489, 545, 584 and 629 nm, which can be attributed from the $^5D_4 \rightarrow {}^7F_j$ (j=6–3) transitions of Tb^{3+}.[46] In particular, the CSS nanoparticles containing $NaGdF_4$:15Tb as the luminescent shell showed maximum radioluminescence intensity, as the result of undesired energy migration associated with a higher concentration of Tb^{3+} activators.[1, 16] The concentration dependent luminescence quenching pathways such as cross-relaxation and energy migration, create nonradiative energy transfer between luminescence activators leading to a dramatic decrease of the RL efficiency.[16] More specifically, the highly concentrated Tb^{3+} ions tend to cluster together with the intensified resonant energy transfer among Tb^{3+} ions. The boosted ion-ion interaction can increase the probability that $^5D_4$ excitation energy trapped at quenching centers and thus result in significant excitation energy loss.[47, 48] For example, the $^5D_4$

emission quenching occurred when Tb concentration reached at 4 mol% in $Li_2SrSiO_4:Tb^{3+}$ phosphors.[48] Figure 2a showed the RL spectra of three structured nanoparticles including $NaGdF_4$@$NaGdF_4$:15Tb@$NaYF_4$ core/shell/shell, $NaGdF_4$:15Tb@$NaYF_4$ core/shell and $NaGdF_4$@$NaGdF_4$:15Tb core/shell nanoparticles. As expected, the $NaGdF_4$@$NaGdF_4$:15Tb core/shell nanoparticles presented very weak RL emission due to the non-radiative surface quenching.[40] In contrast, significant RL enhancement was detected with the $NaGdF_4$@$NaGdF_4$:15Tb@$NaYF_4$ core/shell/shell and $NaGdF_4$:15Tb@$NaYF_4$ core/shell nanoparticles. The enhanced luminescence output is resultant of the blocking of undesired energy migration to surface quenchers by the $NaYF_4$ passivation shell. Importantly, for $NaGdF_4$@$NaGdF_4$:15Tb@$NaYF_4$ core/shell/shell nanoparticles, the X-ray luminescence intensity at 545 nm is about 2 times that of the conventional $NaGdF_4$:15Tb@$NaYF_4$ core/shell nanoparticles. The X-ray luminescence emission of the $NaGdF_4$@$NaGdF_4$:15Tb@$NaYF_4$ core/shell/shell nanoparticles was also compared with reference organic liquid scintillator p-terphenyl, as displayed in Figure S4. Next, to visualize the X-ray luminescence intensification, the above three structure nanoparticles were dispersed in MQ water and the suspension was then transferred into a 96-well black bottom plate with varied Tb concentrations. The plate was then irradiated (225 kV, 13 mA) using a conformal small-animal irradiation system equipped with a bioluminescence imaging camera (X-RAD SmART, Precision X-Ray). It can be seen from the obtained optical images (Figure 2c), the optical luminescence was mostly evident at higher concentrations of nanoparticles, which coincides with the outlines of each well. To better quantify the intensity of the signals and assess the luminescence efficiency of different nanoparticle systems, the region-of-interest (ROI) analysis was conducted. It was revealed that the measured scintillation light output increases in a concentration-dependent manner (Figure 2b).[24] Furthermore, at the same Tb concentration, the CSS nanoparticles were about 1.84-fold brighter than that of the core/shell counterpart, which is in line with the previous discussion. Several aspects may contribute to the enhancement of RL in the nanoparticles designed with a core/shell/shell geometry. First, owing to the high X-ray absorption coefficient (3.11 cm^2/g at 100 keV), Gd can adeptly absorb the X-ray photons with energies just beyond its K-edge energy (50.3 keV).[49, 50] In the X-ray luminescence emission process, the Gd components are believed to act as the X-ray sensitizer, which transfers the harvested X-ray energy to luminescent centers.[19, 51] With the same concentration of Tb^{3+}, the CSS nanoparticles had about 1.58 times Gd^{3+} present than that of the conventional CS nanoparticles. This implies CSS nanoparticles can induce greater X-ray attenuation. The increased X-ray photon absorptance likely plays a fundamental role in the improved RL emission output.[36, 52] Moreover, in the CSS nanoarchitecture, all the Tb^{3+} dopants (luminescent activators) were spatially confined in the 2 nm interior shell resulting in greatly enhanced energy transfer efficiency.[35] Due to the construction of the ultrathin luminescent shell and energy concentration strategy, the migration of excited *e-h* pairs through the host lattice was largely confined within the luminescent layer and excitation energy depletion via long-range migration was substantially reduced. Consequently, the abundant *e-h* pairs recombine radiatively at the luminescent centers leading to the enhanced RL emission.[15, 53] It has also been noted that isolating the activators (Tb^{3+}) in a separate layer could suppress non-radiative interaction between activators and defect quenchers including inner defects and surface defects.[54]

To produce nanosensitizers with efficient RDT, the RB was selected as the suitable photosensitizer to be integrated with CSS nanoparticles. This choice is mainly due to the absorption of RB, which possesses maximum overlap with the green emission bands of CSS nanoparticles (Figure S5). In addition, all the emitters (Tb^{3+}) were intentionally confined near the particle surface which has been demonstrated to promote the Förster resonant energy transfer (FRET) efficiency and resulting in robust singlet oxygen generation.[36–38] Figure S6 showed the X-ray luminescence decreased remarkably after the RB molecules were conjugated onto the CSS nanoparticles, suggesting the highly efficient energy transfer between the lanthanide activators and photosensitizers.

Benefiting from the close proximity between the activators and photosensitizer, RB can be excited to an excited state (S_1) by the incident photon energy. Following the relaxation of the excited state (S_1) by the intersystem crossing (ISC), the PS continuously deexcite to ground state (S_0) via energy exchange with ground state molecular oxygen ($^3O_2$).[55] Simultaneously, cytotoxic $^1O_2$ was generated, which results in the oxidation of surrounding biomolecules. Hence, the detection of $^1O_2$ directly correlates to the efficacy of the RDT treatment. Here, the generation of $^1O_2$ was assessed using a singlet oxygen scavenger, 1,3-Diphenylisobenzofuran (DPBF). Upon reacting with $^1O_2$, the DPBF can decompose to colorless 1,2-dibenzoylbenzene (DBB), leading to the depletion of the absorbance of DPBF. As shown in Figure 3a and S7a, the absorbance of DPBF continuously decreased as a function of X-ray dose. The RB covalently bonded to CSS nanoparticles exhibited higher DPBF consumption at each X-ray dosage level than those in the pure DPBF solution and physically mixed CSS+ free RB solution. This reveals the enhanced singlet oxygen quantum yield of the CSS-RB nanoconjugates in combination with X-ray irradiation. The single oxygen production in solution was also evaluated using the $^1O_2$ indicator, 9,10-Anthracenediyl-bis(methylene)dimalonic acid (ABDA). The $^1O_2$ could oxidate the ABDA to form endoperoxide products and result in loss of absorbance of ABDA in the near UV region.[56] As seen in Figure S7b, an evident decrease of absorption of ABDA was observed for the CSS-RB nanoconjugates under 4 Gy X-ray irradiation. In contrast, no absorbance decay of ABDA was identified in other groups.

Prior to RDT experiments, the cytotoxicity of the as-prepared RGD-CSS-RB nanoconjugates was evaluated with a panel of cell lines including HepG2, NIH/3T3 and U-87 MG cells. As seen in Figure S8, RGD-CSS-RB with the concentration ranging from 0–200 μg/ml showed negligible toxicity towards all three cell lines after incubation for 24 hours, which indicates the good biocompatibility of the RGD-CSS-RB nanoconjugates. Next, the RDT effects of RGD-CSS-RB nanoconjugates were assessed by investigating the cell viability of U-87 MG, human glioblastoma cells, with varied treatments. Free RB, CSS nanoparticles and RGD-CSS-RB nanoconjugates (200 μg/ml) were incubated with U-87 MG cells for 24 hours, followed by X-ray irradiation (4 Gy). Twenty-four hours later, the AlamarBlue assay was performed to determine cell viability. No obvious cell death was detected from the U-87 MG cells treated with RB and CSS nanoparticles upon X-ray irradiation. This indicates the X-ray and the photosensitizer alone present minimal effect on the destruction of cancer cells. While unsurprising, the viability of U-87 MG cells treated with RGD-CSS-RB + IR decreased sharply to 30.3 ± 1.8%, which confirms the significantly enhanced therapeutic effects of RGD-CSS-RB nanoconjugates upon combination with X-ray

irradiation (Figure 3b). Although increasing cell death was observed with the increasing administration of RGD-CSS-RB, over 50% of U-87 MG cells were killed with a low dose of the nanosensitizers (i.e. 25 μg/ml) and IR exposure. This result reveals the RGD-CSS-RB nanoconjugate possesses encouraging RDT efficacy even at low concentrations. The U-87 MG cells with varied treatments and X-ray irradiation were further co-stained with calcein-AM and propidium iodide (PI) to visualize the live/dead cells (Figure S9). The cells incubated with RB with/without X-ray administration displayed minimal cell death suggesting it can only perform as photosensitizer rather than the radiosensitizer. More importantly, the higher red fluorescence signals were visualized in the RGD-CSS-RB + IR group than that of the CSS-RB + IR group. This observation suggests the RGD peptide can increase the uptake of CSS-RB nanoconjugates by U-87 MG cells. The intracellular distribution of RGD-CSS-RB nanoformulation and intracellular $^1O_2$ generation were then imaged using fluorescence signals from the RB and SOSG, as shown in Figure 3d. After 24 hours incubation, red fluorescence emitted from RB distributed throughout the cell cytoplasm. The RGD functionalized CSS-RB nanoconjugates not only possesses high affinity towards $\alpha_v\beta_3$ integrin but also can be efficiently taken up by the U-87 MG cells ($\alpha_v\beta_3$ integrin - positive) via an integrin mediated endocytosis.[57, 58] Upon X-ray irradiation, the control group exhibited minimal green fluorescence from the single oxygen sensors, as seen in Figure 3d. In contrast, strong SOSG-EP fluorescence signals were detected in the cells treated by the combination of RGD-CSS-RB and ionizing radiation. This demonstrates the X-ray excited intracellular ROS generation capability of the RGD-CSS-RB nanoconjugate.

In addition, a γ-H2AX immunofluorescence staining assay was carried out to evaluate the extent of DNA double-stranded breaks (DSB) following the RDT treatment. Phosphorylated histone H2AX (γ-H2AX) is a sensitive protein biomarker monitoring the DNA damage induced by various genotoxic stresses, such as ionizing radiation. Since the expression of histone γ-H2AX reveals the frequency of DSBs in chromatin induced by RT and PDT, the immunofluorescence intensity of phosphorylated histone H2AX was then measured and quantified as the surrogate marker of DNA double-strand breaks following previous reports.[59, 60] Upon irradiation, remarkedly intense γ-H2AX red fluorescence was observed in the nuclei of cells treated with RGD-CSS-RB, while all other groups either without X-ray exposure or without administration of nanosensitizers exhibited very limited fluorescence (Figure 4a). This indicates by RGD-CSS-RB combined with X-ray irradiation resulted in significant breakage of DNA double strands in the cell nuclei. In terms of quantified fluorescence results (Figure 4b), cells treated with RGD-CSS-RB + IR exhibited significantly higher γ-H2AX fluorescence intensity than that of other groups, further confirming the large amount of ROS produced by RGD-CSS-RB nanoconjugates leads to diminished DNA repair ability in the cytoplasm and increased DNA damage. Taken together, the *in vitro* results support the potential of RGD-CSS-RB nanoplatform for effective RDT.

Conclusions

In summary, we have developed a new RL CSS nanophosphor with luminescent activators (Tb^{3+}) spatially confined in the interior shell. Due to the enhanced X-ray attenuation and energy concentration strategy, the CSS nanoparticles showed improved scintillation

properties. Coupled with a photosensitizer and RGD targeting peptide, the nanoconjugates exhibited efficient uptake by U-87 MG cells and robust intracellular ROS generation upon X-ray irradiation leading to increased DNA damage and cell killing. Further, due to the highly efficacious treatment modality of radiation therapy, the X-ray dosing scheme should be carefully tailored to improve the the likely success of RDT in vivo. This study presents encouraging results of the RGD-CSS-RB nanoplatform and justifies its potential RDT applications.

Experimental

Materials

Gadolinium acetate hydrate $Gd(CH_3CO_2)_3{\cdot}xH_2O$(99.9%), terbium acetate hydrate $Tb(CH_3CO_2)_3{\cdot}xH_2O$ (99.9%), europium acetate hydrate $Eu(CH_3CO_2)_3{\cdot}xH_2O$ (99.9%), and chloroform (99.8%) were purchased from Alfa Aesar. Yttrium acetate hydrate $Y(CH_3CO_2)_3{\cdot}xH_2O$ (99.9%), Sodium hydroxide NaOH (99%), ammonium fluoride NH_4F (99.9%), 1-octadecene (ODE, 90%), and oleic acid (OA, 90%) were purchased from Sigma-Aldrich. Hydrochloric acid solution (HCl, 1.0 N), 1,3-diphenylisobenzofuran (DPBF, 97%) 9,10-Anthracenediyl-bis(methylene)dimalonic acid (ABDA, 90%) and dimethyl sulfoxide (DMSO) were purchased from Fisher Scientific. Singlet Oxygen Sensor Green (SOSG) was obtained from Thermo Fisher Scientific. All the chemicals were used without further purification.

Synthesis of $NaGdF_4$ core nanoparticles.

Briefly, the $NaGdF_4$ core nanoparticles were synthesized following the procedure reported in the literature with modifications.[61] In a typical synthesis, 1 mmol of $Gd(CH_3CO_2)_3{\cdot}H_2O$ were dissolved in a 100 ml three-neck flask containing 6 ml oleic acid and 15 ml octadecene. The mixture was heated to 130 °C under vacuum for 60 min and then cooled down to room temperature naturally under the nitrogen flow. Next, 2.5 mmol of NaOH and 4 mmol of NH_4F were dissolved in the methanol and added to the mixture. Thereafter, the reaction mixture was stirred constantly for overnight at room temperature and then heated to 110 °C for 30 min to remove methanol. After purging with nitrogen, the reaction mixture was heated to 300 °C for 120 min under a nitrogen atmosphere. The obtained core nanoparticles were precipitated and washed three times with ethanol and then dispersed in 10 ml cyclohexane.

Synthesis of $NaGdF_4$@$NaGdF_4$: Tb core/shell nanoparticles.

To prepare $NaGdF_4$@$NaGdF_4$:Tb core/shell nanoparticles, $Gd(CH_3CO_2)_3{\cdot}H_2O$ (x mmol, x= 0.95, 0.9, 0.85, 0.8, 0.7, 0.5) and $Tb(CH_3CO_2)_3{\cdot}H_2O$ (1-x mmol) were dissolved in mixture of 6 ml oleic acid and 15 ml octadecene. The mixture was then heated to 130 °C under vacuum for 60 min to remove residual water and form the transparent oleate precursor. After that, the solution was cooled down to 80 °C and 4 ml of above prepared $NaGdF_4$ core nanoparticles were injected to the solution. The resulting mixture was kept at 80 °C for 30 min under vacuum to remove excess cyclohexane and cooled to room temperature later. Subsequently, 10 ml methanol solution containing 2.5 mmol of NaOH and 4 mmol of NH_4F were injected to the mixture and stirred overnight. Thereafter, the reaction mixture was

initially heated to 110 °C for 30 min to remove methanol and then heated to 300 °C for 2 hours under the nitrogen flow. The products were cooled down to room temperature and precipitated with ethanol. Finally, the obtained core/shell nanoparticles were washed with ethanol for three times and redispersed in 5 ml cyclohexane.

Synthesis of $NaGdF_4$@$NaGdF_4$: Tb@$NaYF_4$ core/shell/shell nanoparticles.

To prepare $NaGdF_4$@$NaGdF_4$: Tb@$NaYF_4$ core/shell/shell nanoparticles, 1 mmol of $Y(CH_3CO_2)_3{\cdot}H_2O$ (99.9%) were dissolved in mixture of 6 ml oleic acid and 15 ml octadecene. The mixture was then heated to 130 °C under vacuum for 60 min to remove residual water and form the transparent oleate precursor. After that, the solution was cooled down to 80 °C and 2 ml of above prepared β-$NaGdF_4$@β-$NaGdF_4$: Tb core/shell nanoparticles were injected to the solution. The resulting mixture was kept at 80 °C for 30 min under vacuum to remove excess cyclohexane and cooled to room temperature later. Subsequently, 10 ml methanol solution containing 2.5 mmol of NaOH and 4 mmol of NH_4F were injected to the mixture and stirred overnight. Thereafter, the reaction mixture was initially heated to 110 °C for 30 min to remove methanol and then heated to 300 °C for 2 hours under the nitrogen flow. The products were cooled down to room temperature and precipitated with ethanol. Finally, the obtained core/shell nanoparticles were washed with ethanol for three times and redispersed in 2 ml cyclohexane.

Synthesis of citrate capped CSS nanoparticles.

1.5 ml sodium citrate solution (0.2 M) was added to a microcentrifuge tube containing 10 mg LF-CSS nanoparticles and the resulting mixture was sonicated at room temperature for 60 min to produce the citrate capped CSS nanoparticles. The CSS@Cit nanoparticles were then isolated via centrifugation at 14000 rpm for 30 min, washed three times with MQ water and ethanol and finally dispersed in 1.5 ml MQ water.

Synthesis of poly-l-lysine (PLL) coated CSS nanoparticles.

First, 750 μl of poly-l-lysine solution (1 mg/ml) was mixed with 750 μl of above prepared CSS@Cit solution. After that, the pH of the mixture was adjusted to 12 using NaOH (1 N) solution and the resulting solution was then sonicated at room temperature for 30 min. The obtained products were washed three times with MQ water and redispersed in water.

Preparation of RGD-CSS-RB nanoconjugates.

In a typical procedure, 1 mg Rose Bengal (RB) was dissolved in 1.5 ml MQ water. Next, DMSO (0.5 ml), EDC (2.7 mg) and NHS (6.1 mg) were added to the mixture and incubated in dark for 2 hours. 500 μl of above prepared RB solution and 100 μl of the sulfo-SMCC cross-linker (1 mg/ml) was then added to 1 ml of the CSS@Cit@PLL nanoparticle suspension (5 mg/ml). The resulting mixture was then vigorously stirred overnight in the dark. The CSS-RB nanoconjugates were washed two times with MQ water to remove the nonbonded RB and SMCC and redispersed in 1 ml MQ water. After that, c(RGDfC) peptides were coupled with CSS-RB via thioether bonds and the resulting RGD-CSS-RB nanoconjugates were purified with MQ water washing several times to remove the unreacted peptides.

Characterization.

Dynamic light scattering (DLS, Malvern Zetasizer NanoDS, Westborough, MA, USA) was employed to measure the hydrodynamic size, zeta potential and polydispersity of the nanoparticles. TEM imaging used a Tecnai F-20 TEM (FEI, Hillsboro, OR, USA) at the accelerating voltage of 200 kV. The TEM specimens were prepared by drop casting a small amount of the nanoparticle colloidal solution onto the copper surface of the Formvar/carbon backed TEM grids (Ted Pella, Redding, CA, U.S.A.) with air drying. The powder XRD patterns were acquired in focused beam (Bragg−Brentano) geometry on a Rigaku Ultima IV X-ray diffraction system (Woodlands, TX, USA) using graphite monochromatized Cu Kα radiation and were recorded over the 2θ range of 10−60°. The functional bands present on the nanoparticles were determined by a Fourier transform Infrared Spectrometer (Nicolet iS5, Thermo Fisher Scientific, U.S.) via an ATR diamond crystal at the range between 4000 and 500 cm −1. The X-ray luminescence spectra were collected using a compact cabinet X-ray system (CellRad, Faxitron) equipped with a StellarNet Silver Nova 200 spectrometer (StellarNet Inc.) and an optic fiber cable (Thorlabs) under ambient conditions. The samples in quartz and disposable cuvettes were placed 13 cm away from the X-ray source, which was operated at the maximum power without the beam broadening filter (130 kV, 5 mA). The integration time was set at 60 s.

Detection of singlet oxygen under X-ray irradiation.

The generation of the singlet oxygen was investigated by using the DPBF and ABDA. In the experiment, 10 μl of DPBF ethanol solution (1 mg/ml) or 10 μM ABDA were added to a 96-well plate containing MQ water, 200 μg/ml CSS-RB and the mixture of LF-CSS and RB. After the irradiation with X-ray, the absorbance signals were recorded using an Infinite M200 Pro plate reader (Tecan US Inc, Morrisville, NC, USA).

In vitro cytotoxicity and cellular uptake study.

To access the cytotoxicity of the CSS-RB nanoconjugate, the U87MG (Human glioblastoma astrocytoma), HepG2 (human liver cancer), and NIH-3T3 (mouse embryo fibroblast cell) were employed. The cells were firstly seeded in 96-well microtiter plates at a density of 5 000/well and allowed to attach for 24 h. Next, the culture medium in each well was replaced with 100 μL of fresh medium containing the various concentration of RGD-CSS-RB nanoconjugates or 10% DMSO. After 24 hours incubation at 37 °C and 5% CO2 that, the cell viabilities were determined using AlamarBlue cell viability reagent (ThermoFisher Scientific, USA), as per the manufacturer’s protocol. To evaluate the cellular uptake of the RGD-CSS-RB nanoparticles, U87MG cells were seeded to each well of a four-well glass chamber slide with 100,000 cells/ml and allowed to adhere for 24 h. After the adhesion, RGD-CSS-RB nanoconjugate solution was added to the wells at the concentration of 40 μg/ml and 200 μg/ml. The U87MG cells were further incubated for 24 hours and washed with PBS for three times after that. The cells were then fixed with 10% phosphate buffered formalin and stained with 4,6-diamidino-2-phenylindole (DAPI) to visualize the nuclei. Finally, the cells were imaged using an EVOS FL Auto Imaging System.

Intracellular singlet oxygen generation.

Typically, the U87MG cells were seeded to each well of a four-well glass chamber slide with 100,000 cells/ml and allowed to attach for 24 h. After the attachment, RGD-CSS-RB nanoconjugate solution was added to the wells at the concentration of 40 μg/ml and 200 μg/ml. The U87MG cells were further incubated for 24 hours and washed with PBS for three times. Following that, 1 μM SOSG reagent was added to each well and incubated for 30 min. After washing with PBS for three times, the cells were fixed with 10% phosphate buffered formalin, stained with DAPI and imaged using an EVOS FL Auto Imaging System.

In vitro RDT study.

Briefly, U87MG cells were firstly plated on 96 well plates at a density of 5000 cells/well and allowed to attach for 24 hours. Next, the cells were washed with PBS for three times and incubated with RGD-CSS-RB nanoconjugates with concentration ranging from 25 μg/ml-200 μg/ml. After 24 hours, the cells were washed three times with PBS and fresh media were added to each well. Following that, the cells were exposed with X-ray irradiation at 4 Gy, incubated for another 24 hours and then the cell viability was assessed using AlamarBlue cell viability reagent (ThermoFisher Scientific, USA). Also, to visualize the in vitro cell death, the U87MG cells cultured in a 6-well plate were treated with different nanoformations and for 4 hours and irradiated subsequently. (4 Gy). After 20 hours, the cells were stained using LIVE/DEAD® Cell Imaging Kit (ThermoFisher Scientific, USA) and imaged using an EVOS FL Auto Imaging System.

Immunofluorescent γ-H2AX DNA damage assay.

Typically, the U87MG cells were cultured in each well of a four-well glass chamber slide with 100,000 cells/ml for overnight and then treated with RGD-CSS-RB nanoconjugates (200 μg/ml) for 24 hours and followed by X-ray irradiation at 4 Gy. 24 hours later, the cells were fixed using 10% phosphate buffered formalin, co-stained with DAPI and γ-H2AX assay kit and imaged using an EVOS FL Auto Imaging System.

Statistical Analysis.

Data are presented as mean ± standard deviation. Statistical significance was determined with student t-test using the GraphPad Prism 8 software. $p < 0.05$ was considered statistically significant, with further confidence indicated by asterisks (*, $p < 0.05$, **, $p < 0.01$, ***, $p < 0.001$).

Supplementary Material

Refer to Web version on PubMed Central for supplementary material.

Acknowledgements

This work was supported by the NIH NIGMS as a Maximizing Investigators' Research Award 1R35GM119839-01 (C.S.) and Oregon State University College of Pharmacy Start-up Funds. In addition, partial support was provided through the Portland State University (PSU) faculty development program. We also acknowledge the National Science Foundation for XRD instrumentation (NSF-MRI, Award Number DMR-0923572). We gratefully acknowledge the laboratory facilities and equipment support provided by the PSU Center for Electron Microscopy & Nanofabrication.

References

1. Zhang W, Zhang X, Shen Y, Shi F, Song C, Liu T, Gao P, Lan B, Liu M and Wang S, Biomaterials, 2018, 184, 31–40. [PubMed: 30195803]
2. Zhang X, Lan B, Wang S, Gao P, Liu T, Rong J, Xiao F, Wei L, Lu H and Pang C, Bioconjugate chemistry, 2019, 30, 2191–2200. [PubMed: 31344330]
3. Naczynski DJ, Sun C, Turkcan S, Jenkins C, Koh AL, Ikeda D, Pratx G and Xing L, Nano Lett, 2015, 15, 96–102. [PubMed: 25485705]
4. Naczynski DJ, Stafford JH, Turkcan S, Jenkins C, Koh AL, Sun C and Xing L, Mol Imaging, 2018, 17, 1536012118799131. [PubMed: 30246593]
5. Smith AM, Mancini MC and Nie S, Nat Nanotechnol, 2009, 4, 710–711. [PubMed: 19898521]
6. Pratx G, Carpenter CM, Sun C, Rao RP and Xing L, Opt Lett, 2010, 35, 3345–3347. [PubMed: 20967061]
7. Pratx G, Carpenter CM, Sun C and Xing L, IEEE Trans Med Imaging, 2010, 29, 1992–1999. [PubMed: 20615807]
8. Kamkaew A, Chen F, Zhan Y, Majewski RL and Cai W, ACS Nano, 2016, 10, 3918–3935. [PubMed: 27043181]
9. Sun W, Zhou Z, Pratx G, Chen X and Chen H, Theranostics, 2020, 10, 1296–1318.
10. Fan W, Tang W, Lau J, Shen Z, Xie J, Shi J and Chen X, Adv Mater, 2019, 31, e1806381. [PubMed: 30698854]
11. Zhao J, Duan L, Wang A, Fei J and Li J, Wiley Interdisciplinary Reviews: Nanomedicine and Nanobiotechnology, 2020, 12, e1583. [PubMed: 31566931]
12. Chen H, Gu Z, An H, Chen C, Chen J, Cui R, Chen S, Chen W, Chen X and Chen X, Science China Chemistry, 2018, 61, 1503–1552.
13. Wang Y, Zhao J, Chen Z, Zhang F, Wang Q, Guo W, Wang K, Lin H and Qu F, Biomaterials, 2019, 217, 119282. [PubMed: 31260884]
14. Jacques SL, Physics in Medicine & Biology, 2013, 58, R37. [PubMed: 23666068]
15. Sudheendra L, Das GK, Li C, Stark D, Cena J, Cherry S and Kennedy IM, Chem Mater, 2014, 26, 1881–1888. [PubMed: 24803724]
16. Ou XY, Guo T, Song L, Liang HY, Zhang QZ, Liao JQ, Li JY, Li J and Yang HH, Anal Chem, 2018, 90, 6992–6997. [PubMed: 29757612]
17. Cooper DR, Capobianco JA and Seuntjens J, Nanoscale, 2018, 10, 7821–7832. [PubMed: 29664089]
18. Wegh RT, Donker H, Oskam KD and Meijerink A, Science, 1999, 283, 663–666. [PubMed: 9924020]
19. Zhang W, Shen Y, Liu M, Gao P, Pu H, Fan L, Jiang R, Liu Z, Shi F and Lu H, ACS Appl Mater Interfaces, 2017, 9, 39985–39993. [PubMed: 29063752]
20. Liu Y, Tu D, Zhu H, Li R, Luo W and Chen X, Adv Mater, 2010, 22, 3266–3271. [PubMed: 20533416]
21. Naccache R, Vetrone F, Mahalingam V, Cuccia LA and Capobianco JA, Chemistry of Materials, 2009, 21, 717–723.
22. Liu K, Dong L, Xu Y, Yan X, Li F, Lu Y, Tao W, Peng H, Wu Y and Su Y, Biomaterials, 2018, 158, 74–85. [PubMed: 29304404]
23. Sun C, Pratx G, Carpenter CM, Liu H, Cheng Z, Gambhir SS and Xing L, Adv Mater, 2011, 23, H195–199. [PubMed: 21557339]
24. Ren Y, Winter H, Rosch JG, Jung K, Duross AN, Landry MR, Pratx G and Sun C, ACS Applied Nano Materials, 2019, 2, 3718–3727.
25. Neufeld MJ, Winter H, Landry M, Goforth AM, Khan S, Pratx G and Sun C, ACS Appl Mater Interfaces, 2020, DOI: 10.1021/acsami.0c06010.
26. Carpenter CM, Sun C, Pratx G, Liu H, Cheng Z and Xing L, Opt Express, 2012, 20, 11598–11604. [PubMed: 22714145]

27. Chen H, Colvin DC, Qi B, Moore T, He J, Mefford OT, Alexis F, Gore JC and Anker JN, J Mater Chem, 2012, 22, 12802–12809. [PubMed: 24520183]
28. Ma L, Zou X, Bui B, Chen W, Song KH and Solberg T, Applied Physics Letters, 2014, 105, 013702.
29. Chen H, Wang GD, Chuang Y-J, Zhen Z, Chen X, Biddinger P, Hao Z, Liu F, Shen B and Pan Z, Nano letters, 2015, 15, 2249–2256. [PubMed: 25756781]
30. Sun W, Shi T, Luo L, Chen X, Lv P, Lv Y, Zhuang Y, Zhu J, Liu F and Chen X, Advanced Materials, 2019, 31, 1808024.
31. Sun W, Luo L, Feng Y, Cai Y, Zhuang Y, Xie RJ, Chen X and Chen H, Angewandte Chemie International Edition, 2019.
32. Sun W, Zhou Z, Pratx G, Chen X and Chen H, Theranostics, 2020, 10, 1296. [PubMed: 31938066]
33. Gargas DJ, Chan EM, Ostrowski AD, Aloni S, Altoe MVP, Barnard ES, Sanii B, Urban JJ, Milliron DJ and Cohen BE, Nature nanotechnology, 2014, 9, 300.
34. Rabouw FT, Prins PT, Villanueva-Delgado P, Castelijns M, Geitenbeek RG and Meijerink A, ACS nano, 2018, 12, 4812–4823. [PubMed: 29648802]
35. Zhang X, Chen W, Xie X, Li Y, Chen D, Chao Z, Liu C, Ma H, Liu Y and Ju H, Angewandte Chemie International Edition, 2019, 58, 12117–12122. [PubMed: 31276281]
36. Siefe C, Mehlenbacher RD, Peng CS, Zhang Y, Fischer S, Lay A, McLellan CA, Alivisatos AP, Chu S and Dionne JA, Journal of the American Chemical Society, 2019, 141, 16997–17005. [PubMed: 31592655]
37. Xu B, Zhang X, Huang W, Yang Y, Ma Y, Gu Z, Zhai T and Zhao Y, Journal of Materials Chemistry B, 2016, 4, 2776–2784. [PubMed: 32263342]
38. Marin R, Labrador-Paéz L, Skripka A, Haro-González P, Benayas A, Canton P, Jaque D and Vetrone F, ACS Photonics, 2018, 5, 2261–2270.
39. Wang F, Deng R and Liu X, Nat Protoc, 2014, 9, 1634–1644. [PubMed: 24922272]
40. Wang F, Wang J and Liu X, Angew Chem Int Ed Engl, 2010, 49, 7456–7460. [PubMed: 20809558]
41. Zhdanov R, Podobed O and Vlassov V, Bioelectrochemistry, 2002, 58, 53–64. [PubMed: 12401571]
42. Babic M, Horák D, Trchová M, Jendelová P, Glogarová K, Lesný P, Herynek V, Hájek M and Syková E, Bioconjugate chemistry, 2008, 19, 740–750. [PubMed: 18288791]
43. Kim T, Lemaster JE, Chen F, Li J and Jokerst JV, ACS nano, 2017, 11, 9022–9032. [PubMed: 28759195]
44. Murthy VS, Cha JN, Stucky GD and Wong MS, Journal of the American Chemical Society, 2004, 126, 5292–5299. [PubMed: 15099114]
45. Dreaden EC, Morton SW, Shopsowitz KE, Choi J-H, Deng ZJ, Cho N-J and Hammond PT, ACS nano, 2014, 8, 8374–8382. [PubMed: 25100313]
46. Li K, Zhang Y, Li X, Shang M, Lian H and Lin J, Physical Chemistry Chemical Physics, 2015, 17, 4283–4292. [PubMed: 25573075]
47. Jia C, Xie E, Peng A, Jiang R, Ye F, Lin H and Xu T, Thin Solid Films, 2006, 496, 555–559.
48. Zhou X, Jiang S, Xiang G, Tang X, Luo X, Li L and Zhou X, Journal of the American Ceramic Society, 2018, 101, 3076–3085.
49. Park J-A, Kim H-K, Kim J-H, Jeong S-W, Jung J-C, Lee G-H, Lee J, Chang Y and Kim T-J, Bioorganic & medicinal chemistry letters, 2010, 20, 2287–2291. [PubMed: 20188545]
50. Matsukiyo H, Watanabe M, Sato E, Osawa A, Enomoto T, Nagao J, Abderyim P, AIzawa K, Hitomi K and Tanaka E, Japanese Journal of Applied Physics, 2010, 49, 027001.
51. Wojtowicz AJ, Nuclear Instruments and Methods in Physics Research Section A: Accelerators, Spectrometers, Detectors and Associated Equipment, 2002, 486, 201–207.
52. Lin X, Chen X, Zhang W, Sun T, Fang P, Liao Q, Chen X, He J, Liu M and Wang F, Nano letters, 2018, 18, 948–956. [PubMed: 29278506]
53. Lempicki A, Wojtowicz A and Berman E, Nuclear Instruments and Methods in Physics Research Section A: Accelerators, Spectrometers, Detectors and Associated Equipment, 1993, 333, 304–311.

54. Ding M, Chen D, Ma D, Dai J, Li Y and Ji Z, Journal of Materials Chemistry C, 2016, 4, 2432–2437.
55. Li B, Lin H, Chen D, Wilson BC and Gu Y, Journal of Innovative Optical Health Sciences, 2013, 6, 1330002.
56. Zhuang W, Yang L, Ma B, Kong Q, Li G, Wang Y and Tang BZ, ACS applied materials & interfaces, 2019, 11, 20715–20724. [PubMed: 31144501]
57. Ruoslahti E, Annual review of cell and developmental biology, 1996, 12, 697–715.
58. Jiang W, Fu Y, Yang F, Yang Y, Liu T, Zheng W, Zeng L and Chen T, ACS applied materials & interfaces, 2014, 6, 13738–13748. [PubMed: 25073123]
59. Hou Y-N, Lavaf A, Huang D, Peters S, Huq R, Friedrich V, Rosenstein BS and Kao J, Radiation research, 2009, 171, 360–367. [PubMed: 19267563]
60. Mahrhofer H, Bürger S, Oppitz U, Flentje M and Djuzenova CS, International Journal of Radiation Oncology* Biology* Physics, 2006, 64, 573–580.
61. Wang F, Deng R and Liu X, Nature protocols, 2014, 9, 1634. [PubMed: 24922272]

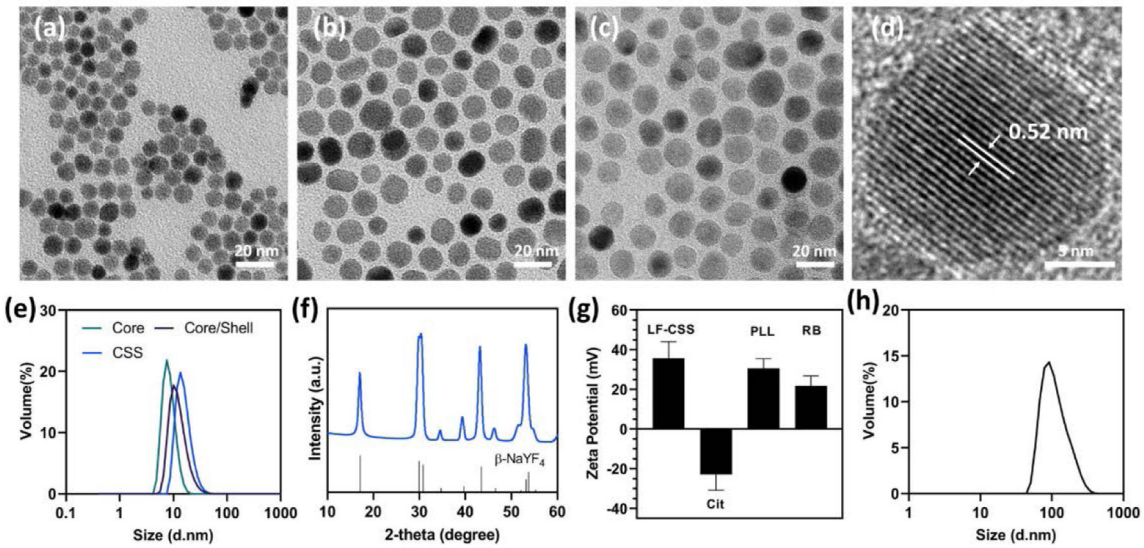

Figure 1.

TEM images of (a) $NaGdF_4$ core, (b) $NaGdF_4$@$NaGdF_4$:Tb core/shell and (c) $NaGdF_4$@$NaGdF_4$:Tb@$NaYF_4$ core/shell/shell (CSS) nanoparticles. (d) HRTEM image of $NaGdF_4$@$NaGdF_4$:Tb@$NaYF_4$ core/shell/shell (CSS) nanoparticles. (e) Size evolution of the CSS nanoparticles measured by DLS. (f) XRD pattern of the as-prepared CSS nanoparticles. (g) zeta-potential measurements at each step in the layer-by-layer coating process. (h) DLS profile of CSS-RB nanoconjugates in MQ water.

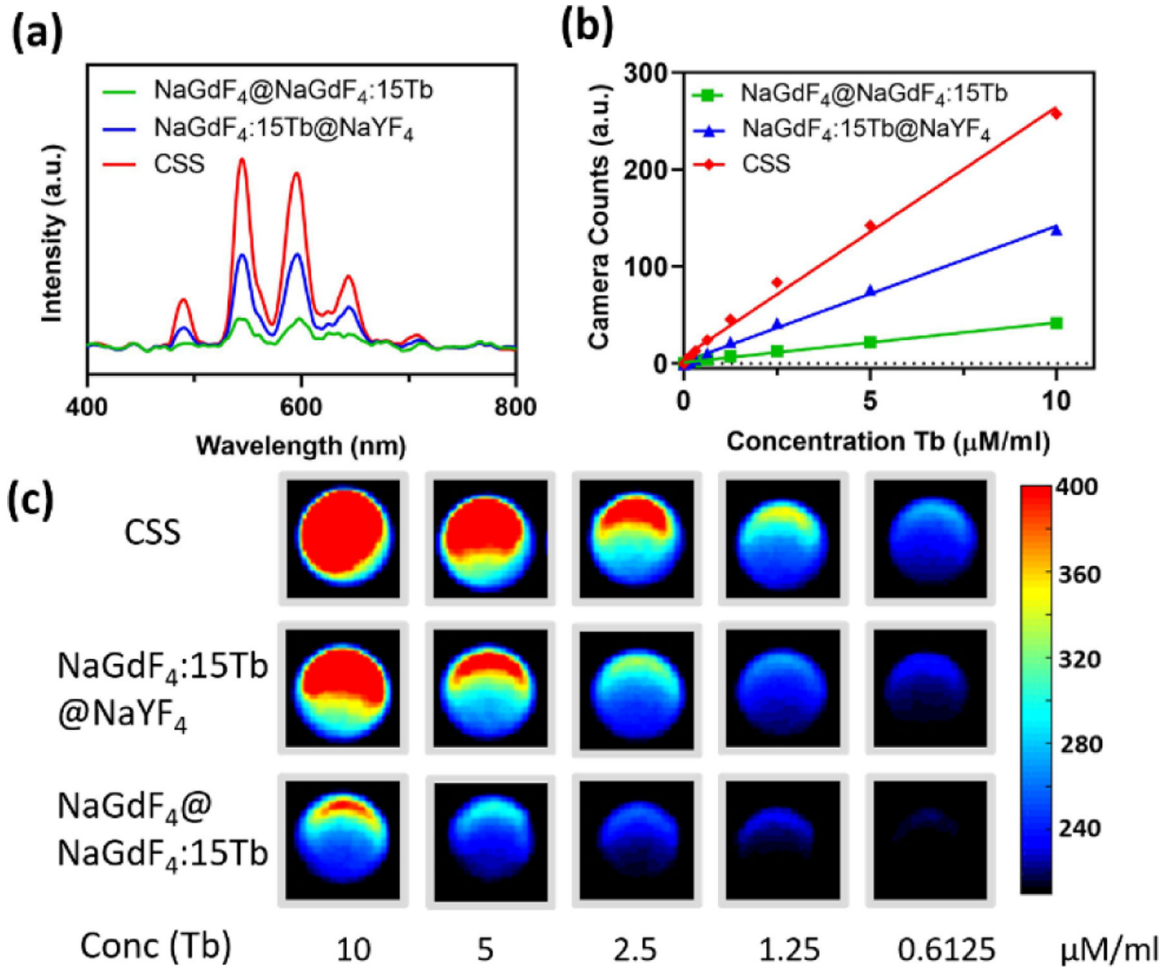

Figure 2.

(a) X-ray excited luminescence spectra of the nanoparticles with varied nanostructures. (b) Camera counts of the $NaGdF_4$@$NaGdF_4$:15Tb, $NaGdF_4$:15Tb@$NaYF_4$ and $NaGdF_4$@$NaGdF_4$:15Tb@$NaYF_4$ water suspensions as a function of the Tb concentration in solution. (c) X-ray excited optical phantom imaging of the aqueous solution of $NaGdF_4$@$NaGdF_4$:15Tb, $NaGdF_4$:15Tb@$NaYF_4$ and $NaGdF_4$@$NaGdF_4$:15Tb@$NaYF_4$ nanoparticles.

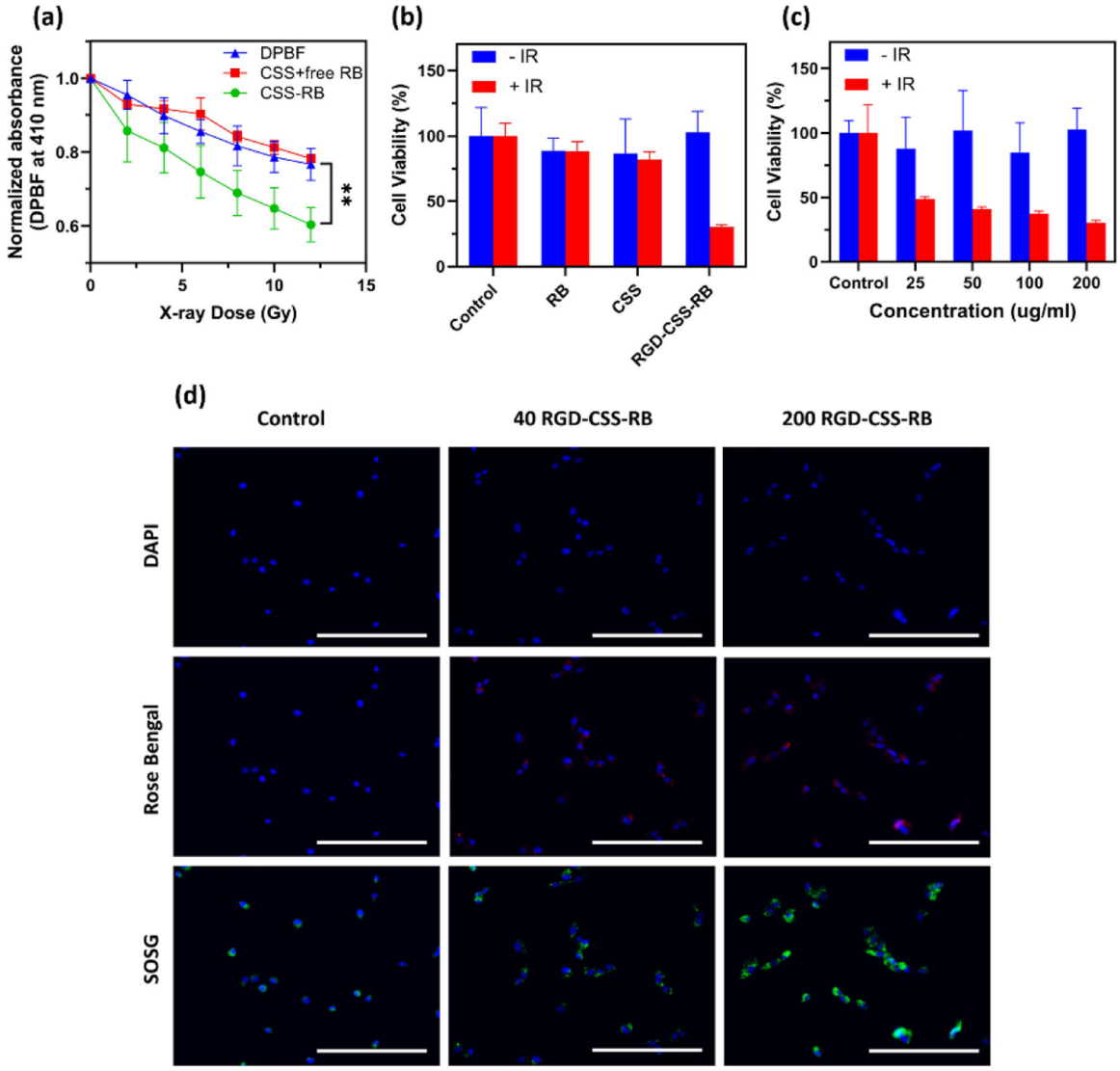

Figure 3.

(a) Decay profiles of the absorbance of DPBF centered at 410 nm in the presence of CSS-RB nanoconjugates, CSS nanoparticles and free Rose Bengal in ethanol/water solution irradiated with increasing X-ray doses. (b) Cell viability of U87 MG cells incubated with RB, CSS and RGD-CSS-RB with or without X-ray irradiation (4 Gy). (c) Cell viability of U-87 MG cells treated with varying amounts of RGD-CSS-RB in the presence or absence of X-ray irradiation (4 Gy). (d) Fluorescence images to show the uptake of RGD-CSS-RB (40 and 200 μg/ml) and X-ray induced intracellular $^1O_2$ generation after incubation with U-87 MG cells for 24 hours. Scale bar represents 200 μm.

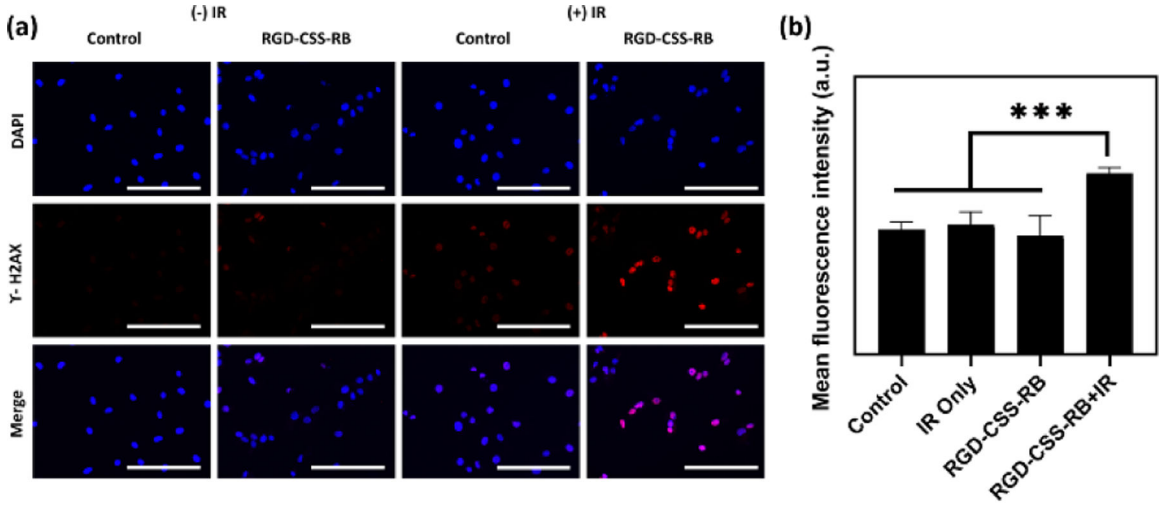

Figure 4.

(a) Representative immunofluorescence images with the γ-H2AX staining assay to highlight the DNA damage after different treatments. Scale bar represents 200 μm. (b) Mean fluorescence intensity results show the increased DNA damage resulted by the combination of RGG-CSS-RB and X-ray irradiation (4 Gy).

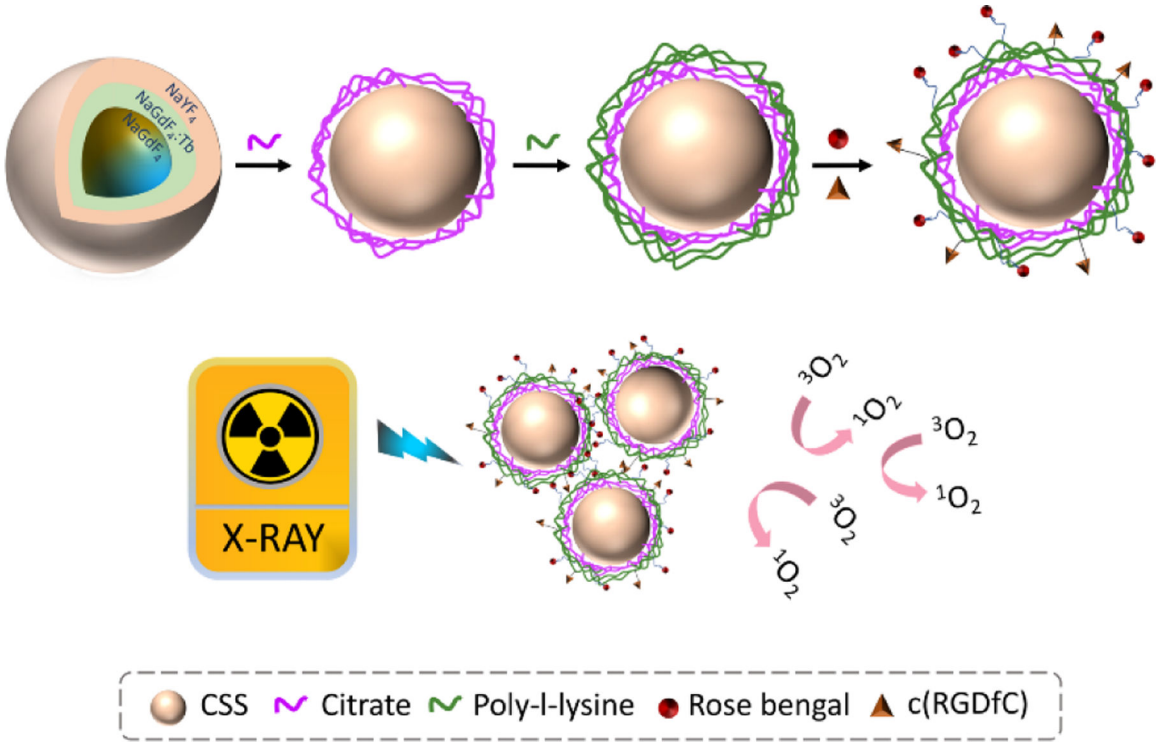

Scheme 1.

The schematic presentation for synthesis of RGD-CSS-RB nanoconjugates and the mechanism of X-ray inducible ROS generation.